Linked skyrmions in shifted magnetic bilayer

Sumit Ghosh,[1,*] Hiroshi Katsumoto,[2] Gustav Bihlmayer,[2] Moritz Sallermann,[2,3,4] Vladyslav M. Kuchkin,[5] Filipp N. Rybakov,[6] Olle Eriksson,[6] Stefan Blügel,[2] and Nikolai S. Kiselev[2]

[1] *The Institute of Physics of the Czech Academy of Sciences, 162 00 Prague, Czech Republic*
[2] *Peter Grünberg Institut (PGI-1), Forschungszentrum Jülich GmbH, 52428 Jülich, Germany*
[3] *Department of Physics, RWTH Aachen University, 52056 Aachen, Germany*
[4] *Science Institute and Faculty of Physical Sciences, University of Iceland, 107 Reykjavík, Iceland*
[5] *Department of Physics and Materials Science, University of Luxembourg, L-1511 Luxembourg, Luxembourg*
[6] *Department of Physics and Astronomy, Uppsala University, SE-75120 Uppsala, Sweden*

We present a shifted magnetic bilayer that exhibits various magnetic phases and magnetic textures with arbitrarily large topological numbers. The proposed system is characterised by a mutually orthogonal Dzyaloshinskii-Moriya interaction (DMI) in two different layers which can be induced by suitably placing non-magnetic atom with spin-orbit coupling. At weak interlayer coupling, the ground state resembles a *checker-board* pattern containing regions with unfavourable magnetic alignment which we call *anti-aligned* points. At finite interlayer coupling and finite external magnetic field, the bilayer can demonstrate a new class of magnetic solitons where multiple magnetic solitons can be connected by topological point defects which we call *linked skyrmion*. In addition to that the model also demonstrates conventional *skyrmion-bags* and $k\pi$-skyrmions. Finally, with rigorous first principle calculations, we propose a suitable material candidate where these magnetic configurations can be observed.

I. INTRODUCTION

Magnetic solitons[1,2] are localised magnetic textures which behave like classical particles and can be characterised by a topological index. Their intricate feature has stimulated a large number of studies in recent years leading to the discovery of unconventional new magnetic texture both in two dimensions[3–6] and three dimensions[7–11]. They can be moved with external charge current[12,13] which makes them a fitting candidate for data storage devices[14–16]. In this regard, the two-dimensional configurations are more promising[17,18] due to their compatibility with current device architecture.

In condensed matter system, the most common example of magnetic solitons are the *skyrmions*[19,20] which is characterised by an integer topological index given by

$$Q = \frac{1}{4\pi}\int dx\ dy\ \mathbf{m}\cdot[\partial_x\mathbf{m}\times\partial_y\mathbf{m}], \qquad (1)$$

where $\mathbf{m}$ is the unit vector denoting the magnetisation direction. This is also known as the topological charge of the corresponding magnetic texture or simply the skyrmion charge. While most of the studies are focused on the skyrmions with $|Q|$=1, recently composite skyrmions with arbitrary large topological charge[4,5], commonly known as skyrmion bags, have also been observed experimentally[21–25]. These complex magnetic textures arise from the competition of different magnetic interactions among which the most prominent ones are the Heisenberg exchange and the Dzyaloshinskii-Moriya interaction (DMI)[26,27]. The interplay between these interactions along with an external magnetic field can result in different types of magnetic solitons.

In this paper, we propose an alternative class of complex magnetic solitons with arbitrarily large topological charge which can be realised in a shifted magnetic bilayer. Our model consists of two magnetic layers where the DMI in each layer is mutually perpendicular to each other (Fig. 1). Such configuration can be achieved by the proximity of a nonmagnetic layer with suitable spin-orbit coupling (SOC). The interlayer coupling can be controlled by using a suitable nonmagnetic spacer. With such anisotropic DMI and an external magnetic field, the proposed bilayer can demonstrate a wide variety of complex solitons along with the existing bag-like skyrmions. By analysing its phase space, we show the suitable parameter region to obtain complex textures with higher topological charges and establish their topological stability with homotopy group analysis. Finally, with a sys-

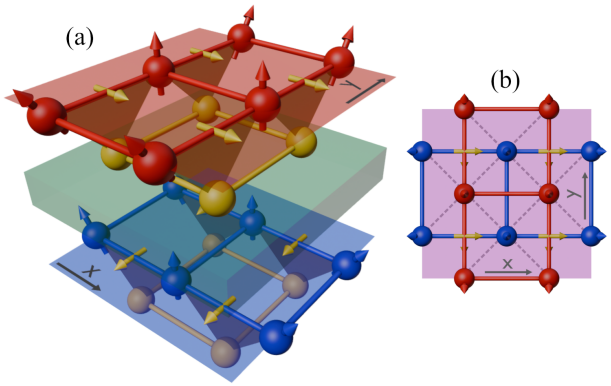

FIG. 1. Schematic of the shifted magnetic bilayer. (a) Red, blue and yellow spheres show the top magnetic, bottom magnetic and non-magnetic sites. Resulting direction of the DMI vectors are shown with yellow arrows. Red and blue arrows show the favourable orientation of the spin due to the DMI. Green region shows the nonmagnetic spacer layer. (b) Top view of the bilayer. Dashed lines show the nearest neighbours from opposite layers.

tematic first-principle study, we propose a suitable combination of materials where such complex solitons can be observed.

II. SHIFTED MAGNETIC BILAYER

Our system is composed of two magnetic layers made of square lattices (the lattice constant is chosen to be 1) such that the centre of the top and bottom layers are shifted by (1/2,1/2) (Fig. 1) like a Zincblende structure. A square lattice of nonmagnetic material as a source of SOC is placed such that the centre of this lattice is shifted by (1/2,0) from the bottom layer and (0,1/2) from the top layer (Fig. 1). The structural symmetry gives rise to DMI along specific directions only[14,28] as shown in Fig. 1. There might be a small induced DMI in the other direction and along the interlayer bonds which, without loss of generality is set to zero. For simplicity, we also ignore the effect of any magneto-crystalline anisotropy which does not change the qualitative nature of the outcomes. The direction of the dominant DMI vector ($\boldsymbol{d}_{ij}$) along the line $\boldsymbol{r}_{ij}$ connecting site i and j for top(T) and bottom(B) layers are defined as

$$\boldsymbol{d}_{ij}^{\mathrm{T}} = \begin{cases} 0, & \boldsymbol{r}_{ij} \parallel \boldsymbol{e}_x, \\ \boldsymbol{e}_x, & \boldsymbol{r}_{ij} \parallel \boldsymbol{e}_y, \end{cases} \quad \boldsymbol{d}_{ij}^{\mathrm{B}} = \begin{cases} -\boldsymbol{e}_y, & \boldsymbol{r}_{ij} \parallel \boldsymbol{e}_x, \\ 0, & \boldsymbol{r}_{ij} \parallel \boldsymbol{e}_y, \end{cases} \tag{2}$$

and the complete lattice magnetic Hamiltonian for the bilayer is given by

$$\begin{aligned} \mathcal{H} = & -J \sum_{\langle ij \rangle; l} \boldsymbol{m}_i^l \cdot \boldsymbol{m}_j^l - D \sum_{\langle ij \rangle; l} \boldsymbol{d}_{ij}^l \cdot (\boldsymbol{m}_i^l \times \boldsymbol{m}_j^l) \\ & - J_{\mathrm{C}} \sum_{\langle i'j' \rangle} \boldsymbol{m}_{i'}^{\mathrm{T}} \cdot \boldsymbol{m}_{j'}^{\mathrm{B}} - \mu B_{\mathrm{ext}} \sum_{i;l} \boldsymbol{e}_z \cdot \boldsymbol{m}_i^l, \end{aligned} \tag{3}$$

where $\langle ij \rangle$ indicates summation over the nearest neighbours in the same layer and $\langle i'j' \rangle$ corresponds to the summation over the nearest neighbours of different layers. The superscript l runs over the top(T) and bottom (T) layer. J and J_C correspond to the Heisenberg exchange parameter in the same and different layers respectively and D is the magnitude of DMI. Here we consider $J, J_C > 0$ resulting in a ferromagnetic coupling and D=0.2J. We consider the same J, J_C along both x and y direction which is a valid assumption for $J_C << J$. The model, therefore, can be considered as two mono-axial chiral magnets[29] coupled by the ferromagnetic interlayer exchange (J_C). μ is the saturation magnetisation which we set to 1 and B_{ext} is the external magnetic field applied along z axis.

III. PHASE DIAGRAM

The phase diagram of the system is constructed by varying the interlayer coupling J_C and external field B_{ext} (Fig.2). In the absence of any interlayer coupling (J_C=0) and external magnetic field (B_{ext}=0), the ground state of the system is made of spin spirals with q vector $|\boldsymbol{q}_{\mathrm{B,T}}|=D/J$. For our choice of parameters, the optimal wavelength of such a spin spiral is $L_D=2\pi/|\boldsymbol{q}_L|$=31.5 which is also reflected in our numerical simulation. When viewed together as a bilayer, the superimposed spirals create a checker-board pattern and therefore we call this phase *checker board* phase (Fig.2d-f). This phase remains the ground state for small J_C ($J_{\mathrm{C}}/J \lesssim 0.01$). An interesting feature of the checker-board phase which distinguishes it from the earlier mono layer checker board configuration formed by multi-q spin waves,[30] is the presence of points where the top and bottom layers are aligned against the direction favoured by the interlayer exchange (marked by orange circles in Fig.2b,d-f). We call these points *anti-aligned* points. In the following section, we will show that these points play a crucial role in the formation of linked skyrmions and can be characterised as topological defects. With the increase of interlayer coupling, such points become less favourable and the ground state is made of spin spirals where the $(\boldsymbol{q}_{\mathrm{T}} \rightarrow \boldsymbol{q}_{\mathrm{B}}) || \boldsymbol{e}_x \pm \boldsymbol{e}_y$. With the increase of the external magnetic field, the ground state is gradually made of skyrmion lattice. Unlike the checker-board or the spiral phase, the skyrmion lattice phase can be characterised by a non-zero topological charge (Eq.1) where the skyrmion domain is the unit cell of the lattice (denoted by the dashed line in Fig. 2g). For convenience, we define a layer-resolved topological charge

$$Q_{\mathrm{T,B}} = \frac{1}{4\pi} \int dx\ dy\ \mathbf{m}^{\mathrm{T,B}} \cdot [\partial_x \mathbf{m}^{\mathrm{T,B}} \times \partial_y \mathbf{m}^{\mathrm{T,B}}], \tag{4}$$

In case of the skyrmion lattice, the integration is done over a finite region marked by dashed line in Ref. 2g which gives Q_{T}=Q_{B}=-1.

Along with the skyrmion lattice, a large variety of complex metastable states with arbitrarily large topological charges can also coexist within the same parameter region which is elaborated in the next sections. These states are broadly classified into two classes - (i) Linked skyrmions and (ii) Skyrmion bags and kπ-skyrmions. In case of a linked skyrmion one can have both $Q_{\mathrm{T}} \neq Q_{\mathrm{B}}$ and Q_{T}=Q_{B} with one or multiple point defect whereas for the kπ-skyrmion and skyrmion bags always have Q_{T}=Q_{B} and no point defect.

A. Linked Skyrmion

The transition from the checker-board phase to the skyrmion lattice phase is achieved by increasing the interlayer coupling and applying an external field. This makes the *anti-aligned* points energetically unfavourable. However, survival of an *anti-aligned* point leads to the formation of a new class of magnetic texture where one may have $Q^{\mathrm{T}} \neq Q^{\mathrm{B}}$ which we call a *linked skyrmion* (Fig. 3). Such configurations are observed over a wide range in the

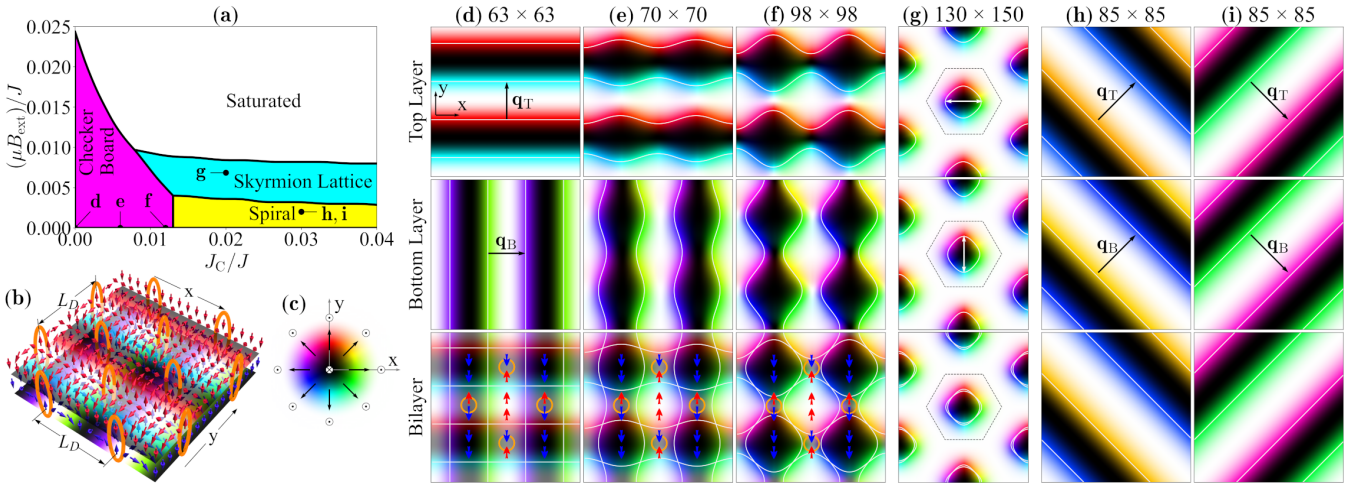

FIG. 2. Phase diagram and different periodic ground states of the bilayer Hamiltonian (Eq.3). (a) Phase diagram showing checker-board (magenta), spiral (yellow), skyrmion lattice (cyan) and saturated ferromagnetic (white) phase and the location of the representative configurations. (b) Schematic of the checker board in the decoupled limit (J_C=0) and in absence of external magnetic field ($B_{\rm ext}$=0). Orange ellipses show the *anti-aligned* points. (c) Colour code used in the figures demonstrated with an isotropic Néel skyrmion. ⊙(⊗) shows the region with positive(negative) out of plane components denoted by black(white) colour. Layer resolved checker-board pattern with $B_{\rm ext}$=0.0 and (d)J_C=0.0J, (e)J_C=0.006 and (f)J_C=0.012J. $\boldsymbol{q}_{\rm T,B}$ shows the direction of the spiral q vector in top,bottom layer. The numbers on the top show the optimal cell size. White lines show the trajectory of the zero out-of-plane magnetisation. Orange circles show the location of the *anti-aligned* points and red and blue arrows show the out of plane magnetic alignment from top and bottom layer in the corresponding region. (g) Skyrmion lattice phase obtained at (J_C=0.02J,$\mu B_{\rm ext}$=0.007J). The hexagonal region denotes the domain of the skyrmion (Eq.1) and the white arrows show the elongation of the skyrmion in individual layers. (h,i) Show two degenerate spin spiral configurations obtained at (J_C=0.03J,$\mu B_{\rm ext}$=0.002J).

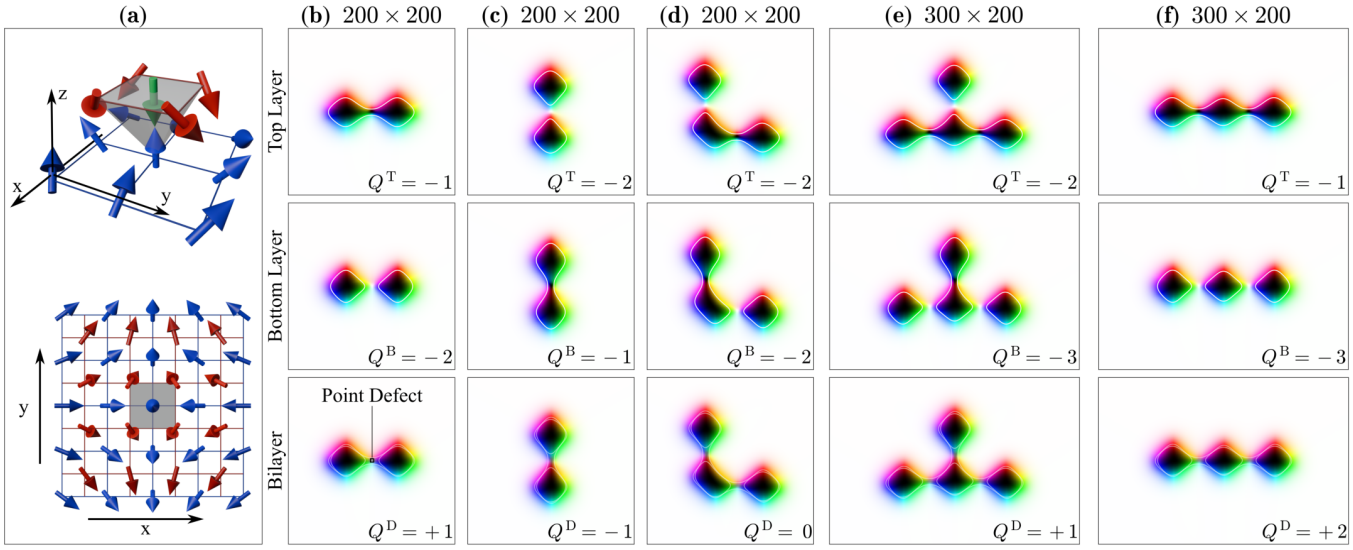

FIG. 3. Linked skyrmion with different topological charges. (a) Enlarged view of the topological point defect. Red and blue arrows show the magnetic moment on top and bottom layer. The green arrow shows the average of the four magnetic moments of the top layer which constitutes the *anti-aligned* point confined within the grey region. Bottom panel shows the top view of the extended region containing the point defect where the grey box denotes the region of the *anti-aligned* point. (b-f) Different linked skyrmions with their topological charge from top ($Q^{\rm T}$) and bottom ($Q^{\rm B}$) layer and the corresponding charge of the topological point defect ($Q^{\rm D}$). All configurations are stabilised at (J_C=0.02J,$\mu B_{\rm ext}$=0.007J) in a 400×400 mesh. The number on the top shows the dimesnsion of the plotting region. The small square region of the bottom panel of column (**b**) correspond to the configuration at the bottom panel of column (**a**).

phase space where skyrmion lattice is observed. In Fig. 3 we use J_C/J=0.02 and $\mu B_{ext}/J$=0.007 which are the

same values used to stabilise skyrmion lattice (Fig. 2g). Such texture can have any number of skyrmions in each layer resulting in an arbitrarily large topological charge.

Topological nature of the skyrmion links: At the centre of each skyrmion link, lies an *anti-aligned* point. As a result, the average magnetisation of the bilayer in the surrounding region tends to be zero. Thus, the texture in Fig. 3a can be considered to contain a point defect. Similar to the Bloch point[31] - a magnetic point defect in bulk crystals - the *anti-aligned* points can also be characterized by a topological charge, Q^{D} which differs from the skyrmion topological charge (see Supplementary materials S1). Here, the topological charge of such a point defect can be expressed in terms of the skyrmion topological charges in the top and bottom layers as

$$Q^{\mathrm{D}} = Q^{\mathrm{T}} - Q^{\mathrm{B}}. \tag{5}$$

For the linked-skyrmions, therefore, it is specifically the difference of Q^{T} and Q^{B} that serves as a meaningful classifying quantity.

IV. SKYRMION BAGS AND $k\pi$-SKYRMIONS

The other class of configuration present in the same region of the phase space contains textures with Q^{T}=Q^{B} and consequently Q^{D}=0 (Fig. 4). We use J_C/J=0.02 and $\mu B_{ext}/J$=0.007 for comparing them with skyrmion lattice and linked skyrmions. These textures can be further divided into two subclasses namely skyrmion bags[4,5] and so-called $k\pi$-skyrmions[32]. Note that, unlike the linked skyrmion, here the total topological charge can be both positive or negative as well as zero.

V. MATERIAL REALISATION

We have conducted a thorough first principle study to identify a suitable material for this system. Our studies show that the thin-film structure of Ni/InAs(001) can be an ideal candidate which possesses all the relevant symmetry and necessary DMI (Fig. 5). The exchange and DMI along x and y direction are obtained from the total energy of the spin spiral with different q vectors (Fig. 5b) (See Supplementary S2 for details). Although our calculation shows the existence of finite exchange and DMI beyond the first nearest neighbours (see Supplementary Materials S2 for details), the dominant contribution comes from the first nearest neighbours. Considering the leading order contribution, for the top layer we find that J_x=1.4meV, D_x=0meV and J_y=1.6meV, D_y=0.1meV where the suffix denotes the direction of the bond. Due to the symmetry, the bottom layer would have the same magnitude of the J and D parameters with x and y being interchanged.

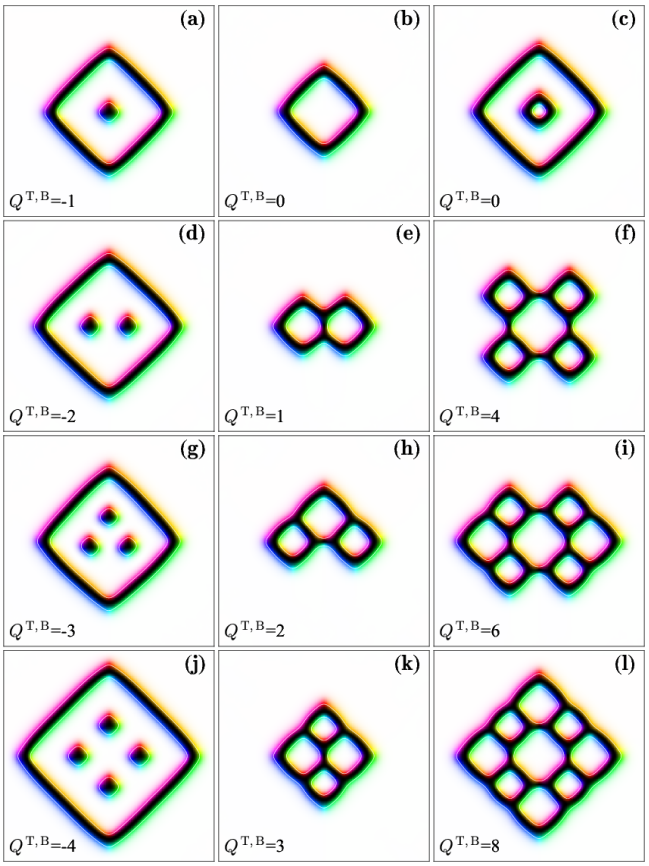

FIG. 4. Different composite skyrmions without point defect. (a-c) $k\pi$-skyrmions and (d-l) skyrmion bags with different topological charges stabilised at (J_C=0.02J,μB_{ext}=0.007J) in a 400×400 mesh. The figures present the total magnetisation of both layers. The legends show the topological charge from top and bottom layer.

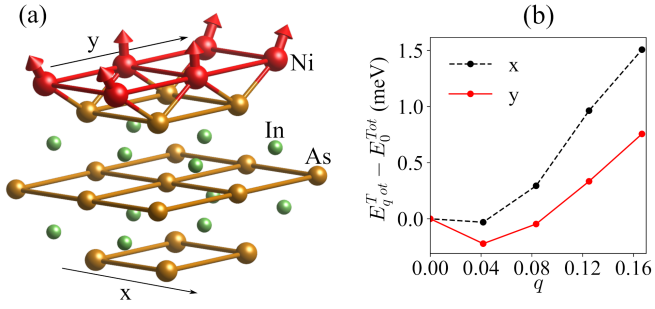

FIG. 5. Material realisation of the bilayer model. (a) The thin-film structure of Ni/InAs(001). Red spheres denote Ni (magnetic) layer and yellow spheres denote In (main source of SOC). As is shown in green. (b) Total energy of spin spiral where red and black dashed lines represent spiral along y and x direction on the top layer.

VI. CONCLUSIONS

In this work, we present a shifted magnetic bilayer that hosts a wide range of magnetic configurations which can be obtained by tuning the interlayer exchange coupling and external magnetic field. One of the most interesting features is the presence of special regions where the interlayer magnetic alignment is opposite to the direction favoured by the interlayer exchange. We call these points *anti-aligned* points which play a crucial role in connecting multiple solitons creating a new class of complex magnetic texture with an arbitrary large topological index which we call *linked skyrmion*. Homotopy group analysis shows that these points are topologically stable. Finally, we propose suitable materials based on first principle calculation where such solitons can be observed. We show a specific example with Ni/InAs(001) thin film which possesses all necessary symmetry and interactions. The interlayer coupling can be tuned by controlling the thickness of the InAs layers and also by inserting suitable non-magnetic layer. Since the theoretical model is quite general, there are a large class of materials which can satisfy the necessary symmetry requirements to realise our finding. Our studies, therefore can open new possibilities in engineering higher order topological solitons.

VII. METHOD

A. Atomistic simulation

The atomistic simulation is done with the atomistic simulation code Spirit[33]. The optimised solutions are obtained by minimising the energy with a threshold of $10^{-10}J$. In case of periodic configurations shown in Fig.2d-i the optimum system size is obtained by varying the dimension by and finding the dimension corresponding to the minimum energy for each set of parameters. For the isolated solitons (Fig.3,4) we use D=0.2J, J_C=0.02J and B_{ext}=0.007J and a mesh size of 400×400 to avoid finite size effects.

B. Homotopy-group analysis

Following the approach proposed in[34,35], we first define an effective space for the order parameter by analysing the most unfavourable spin orientations (See Supplementary S1 for details) as

$$X = \left\{(\boldsymbol{m}^{\mathrm{T}}, \boldsymbol{m}^{\mathrm{B}});\, \boldsymbol{m}^{\mathrm{T}} \in \mathbb{S}^2,\, \boldsymbol{m}^{\mathrm{B}} \in \mathbb{S}^2,\, \boldsymbol{m}^{\mathrm{T}} \neq -\boldsymbol{m}^{\mathrm{B}}\right\}. \quad (6)$$

Note that X is the homotopy equivalent to $\mathbb{S}^2$. Considering the first homotopy group $\pi_1(X)$=$\pi_1(\mathbb{S}^2)$=0, one can see that there are no stable vortices in this system. Each layer can have ordinary skyrmions corresponding to the map $I^2/\partial I^2 \to \mathbb{S}^2$, where I^2 is a rectangle and ∂I^2 is its perimeter. The corresponding topological charges of the skyrmions in each layer are given by

$$Q^{\mathrm{L}} = \frac{1}{4\pi}\int dS\ \mathbf{F}^{\mathrm{L}} \cdot \hat{\mathrm{e}}_z, \quad (7)$$

where F_z^{L}=$\boldsymbol{m}^{\mathrm{L}} \cdot (\partial_x \boldsymbol{m}^{\mathrm{L}} \times \partial_y \boldsymbol{m}^{\mathrm{L}})$ and L=T,B represents the top and the bottom layers. In addition to that, the system can have stable point defects corresponding to the second homotopy group $\mathbb{S}^2 \to \mathbb{S}^2$, $\pi_2(\mathbb{S}^2) = \mathbb{Z}$. The preimage of the map is a closed surface of containing a point defect (See Fig.3). The topological charge of this point defect can be defined by the Kronecker integral

$$Q^{\mathrm{D}} = \frac{1}{4\pi}\oiint dS\ \boldsymbol{F} \cdot \hat{\boldsymbol{n}}, \quad (8)$$

where $\hat{\boldsymbol{n}}$ is the unit normal to the surface and $\boldsymbol{F}$ is the vector curvature. For a trapezoidal volume around the point defect, we have $\hat{\boldsymbol{n}}^{\mathrm{T}}$=-$\hat{\boldsymbol{n}}^{\mathrm{B}}$=$\hat{e}_z$. Using Eq.7 and keeping in mind that the net contribution from the side surfaces vanishes, we obtain

$$Q^D = Q^{\mathrm{T}} - Q^{\mathrm{B}} \quad (9)$$

which represents the topological point defect as the difference of the stable skyrmion topological charges of the individual layers.

C. First principle calculation

The first principle calculation is done with the ab initio code FLEUR[36] (See Suppl.S2 for details). Here we use a symmetric thin film structure with a in-plane lattice vector 4.27Å. The Heisenberg exchange (J) and DMI (D) parameter is obtained from the energy of the spin spirals along specific direction using generalised Bloch theorem on a 48×48×1 mesh. To obtain J we calculate the energy of the spin spiral along direction $\hat{i}$ without SOC and fit it with $E(q_i)$=$E(-q_i)$=-E_0-$\sum_n J_i^n \cos(2n\pi q_i)$ where J_i^n is the Heisenberg exchange between n^{th} nearest neighbour along $\hat{i}$. For the DMI we calculate the energy due to SOC and fit it with $E_{SOC}(q_i)$=-$E_{SOC}(-q_i)$=-$\sum_n D_i^n \sin(2n\pi q_i)$ where D_i^n is the DMI vector between n^{th} nearest neighbour along $\hat{i}$ direction.

VIII. ACKNOWLEDGEMENT

SG is co-funded by the European Union (Physics for Future – Grant Agreement No. 101081515). This project has received funding from the European Research Council under the European Union's Horizon 2020 Research and Innovation Programme (Grant No. 856538 - project "3D MAGiC"). HK acknowledges computing time on the supercomputer JURECA[37] at Forschungszentrum Jülich under grant no. JIFF38.

IX. AUTHOR CONTRIBUTIONS

SG, HK and SB have initiated the project. SG has established the model and obtained different solutions. HK has conducted the symmetry analysis and carried out the first principle calculation with the help of GB. FR has carried out the homotopy group analysis. VK helped with the phase space analysis. SG has written the manuscript with feedback from others. All co-authors have discussed the results and contributed equally.

* ghoshs@fzu.cz

[1] A. Kosevich, B. Ivanov, and A. Kovalev, Phys. Rep. **194**, 117 (1990).
[2] N. Manton and P. Sutcliffe, *Topological Solitons* (Cambridge University Press, 2004).
[3] S.-Z. Lin, A. Saxena, and C. D. Batista, Phys. Rev. B **91**, 224407 (2015).
[4] D. Foster, C. Kind, P. J. Ackerman, J.-S. B. Tai, M. R. Dennis, and I. I. Smalyukh, Nat. Phys. **15**, 655 (2019).
[5] F. N. Rybakov and N. S. Kiselev, Phys. Rev. B **99**, 064437 (2019).
[6] B. Göbel, I. Mertig, and O. A. Tretiakov, Phys. Rep. **895**, 1 (2021), arXiv:2005.01390.
[7] S. Okumura, S. Hayami, Y. Kato, and Y. Motome, Phys. Rev. B **101**, 144416 (2020).
[8] N. Kent, N. Reynolds, D. Raftrey, I. T. G. Campbell, S. Virasawmy, S. Dhuey, R. V. Chopdekar, A. Hierro-Rodriguez, A. Sorrentino, E. Pereiro, S. Ferrer, F. Hellman, P. Sutcliffe, and P. Fischer, Nature Communications **12** (2021), 10.1038/s41467-021-21846-5.
[9] M. Azhar, V. P. Kravchuk, and M. Garst, Phys. Rev. Lett. **128**, 157204 (2022).
[10] F. Zheng, N. S. Kiselev, F. N. Rybakov, L. Yang, W. Shi, S. Blügel, and R. E. Dunin-Borkowski, Nature **623**, 718 (2023).
[11] Y. Liu and N. Nagaosa, Phys. Rev. Lett. **132**, 126701 (2024).
[12] S. Woo, K. Litzius, B. Krüger, M.-Y. Im, L. Caretta, K. Richter, M. Mann, A. Krone, R. M. Reeve, M. Weigand, P. Agrawal, I. Lemesh, M.-A. Mawass, P. Fischer, M. Kläui, and G. S. D. Beach, Nat. Mater. **15**, 501 (2016).
[13] X. S. Wang, A. Qaiumzadeh, and A. Brataas, Phys. Rev. Lett. **123**, 147203 (2019).
[14] A. Fert, V. Cros, and J. Sampaio, Nat. Nanotechnol. **8**, 152 (2013).
[15] G. Yu, P. Upadhyaya, Q. Shao, H. Wu, G. Yin, X. Li, C. He, W. Jiang, X. Han, P. K. Amiri, and K. L. Wang, Nano Lett. **17**, 261–268 (2016).
[16] B. He, R. Tomasello, X. Luo, R. Zhang, Z. Nie, M. Carpentieri, X. Han, G. Finocchio, and G. Yu, Nano Lett. **23**, 9482 (2023).
[17] A. Fert, N. Reyren, and V. Cros, Nat. Rev. Mater. **2**, 17031 (2017).
[18] K. Everschor-Sitte, J. Masell, R. M. Reeve, and M. Kläui, J. Appl. Phys. **124** (2018), 10.1063/1.5048972.
[19] U. K. Rößler, A. N. Bogdanov, and C. Pfleiderer, Nature **442**, 797–801 (2006).
[20] N. Nagaosa and Y. Tokura, Nat. Nanotechnol. **8**, 899 (2013).
[21] J. Tang, Y. Wu, W. Wang, L. Kong, B. Lv, W. Wei, J. Zang, M. Tian, and H. Du, Nature Nanotechnology **16**, 1086 (2021).
[22] L. Powalla, M. T. Birch, K. Litzius, S. Wintz, F. S. Yasin, L. A. Turnbull, F. Schulz, D. A. Mayoh, G. Balakrishnan, M. Weigand, X. Yu, K. Kern, G. Schütz, and M. Burghard, Advanced Materials **35** (2023), 10.1002/adma.202208930.
[23] Y. Zhang, J. Tang, Y. Wu, M. Shi, X. Xu, S. Wang, M. Tian, and H. Du, Nature Communications **15**, 3391 (2024).
[24] L. Yang, A. S. Savchenko, F. Zheng, N. S. Kiselev, F. N. Rybakov, X. Han, S. Blügel, and R. E. Dunin-Borkowski, Adv. Mater. **2403274**, 1 (2024).
[25] M. Hassan, S. Koraltan, A. Ullrich, F. Bruckner, R. O. Serha, K. V. Levchenko, G. Varvaro, N. S. Kiselev, M. Heigl, C. Abert, D. Suess, and M. Albrecht, Nature Physics **20**, 615–622 (2024).
[26] I. E. Dzialoshinskii, JETP **5**, 1259 (1957).
[27] T. Moriya, Phys. Rev. **120**, 91 (1960).
[28] A. Fert and P. M. Levy, Phys. Rev. Lett. **44**, 1538 (1980).
[29] J.-i. Kishine and A. Ovchinnikov, "Theory of monoaxial chiral helimagnet," in *Solid State Physics* (Elsevier, 2015) p. 1–130.
[30] S. Hayami, Phys. Rev. B **108**, 094415 (2023).
[31] A. P. Malozemoff and J. C. Slonczewski, *Magnetic domain walls in bubble materials: advances in materials and device research* (Academic press, 1979).
[32] A. Bogdanov and A. Hubert, Journal of magnetism and magnetic materials **195**, 182 (1999).
[33] G. P. Müller, M. Hoffmann, C. Dißelkamp, D. Schürhoff, S. Mavros, M. Sallermann, N. S. Kiselev, H. Jónsson, and S. Blügel, Phys. Rev. B **99**, 224414 (2019).
[34] F. N. Rybakov and O. Eriksson, preprint arXiv:2205.15264 (2022), 10.48550/arXiv.2205.15264.
[35] F. N. Rybakov, O. Eriksson, and N. S. Kiselev, Phys. Rev. B **111**, 134417 (2025).
[36] "The FLEUR project," `https://www.flapw.de/`.
[37] P. Thörnig, J. Large-scale Res. Facil. JLSRF **7**, A182 (2021).
[38] C. Kosniowski, *A first course in algebraic topology* (Cambridge University Press, 1980).
[39] J. A. Aminov, Mathematics of the USSR-Sbornik **9**, 199 (1969).
[40] B. Berg and M. Lüscher, Nuclear Physics B **190**, 412 (1981).

Supplementary Materials

S1. HOMOTOPY-GROUP ANALYSIS

A. The fundamental group

First, let us identify the fundamental group of possible topological defects in our system. For every layer considered separately, the order parameter space is $\mathbb{S}^2$, and no stable vortices are expected since $\pi_1(\mathbb{S}^2) = 0$. However, the situation is less evident in the case of two monolayers coupled through the interlayer exchange. Following the approach proposed in Ref.[34], we define an effective space for the order parameter constrained by the model Hamiltonian. For spins from the top and bottom layers and interacting ferromagnetically, the most energetically unfavorable state is antiparallel. Hence, the effective order parameter space along the loop surrounding these defects is

$$X = \{(\boldsymbol{m}^{\mathrm{T}}, \boldsymbol{m}^{\mathrm{B}});\ \boldsymbol{m}^{\mathrm{T}} \in \mathbb{S}^2,\ \boldsymbol{m}^{\mathrm{B}} \in \mathbb{S}^2,\ \boldsymbol{m}^{\mathrm{T}} \neq -\boldsymbol{m}^{\mathrm{B}}\}. \quad (10)$$

The space X is homotopy equivalent to the $\mathbb{S}^2$, which can be explicitly illustrated by the deformation retract[38]. In our case, the space X allows retraction to $\mathbb{S}^2$ and this map can be explicitly written as follows:

$$(\boldsymbol{m}^{\mathrm{T}}, \boldsymbol{m}^{\mathrm{B}}) \mapsto \left(\frac{\boldsymbol{m}^{\mathrm{T}} + \tau \boldsymbol{m}^{\mathrm{B}}}{|\boldsymbol{m}^{\mathrm{T}} + \tau \boldsymbol{m}^{\mathrm{B}}|}, \frac{\boldsymbol{m}^{\mathrm{B}} + \tau \boldsymbol{m}^{\mathrm{T}}}{|\boldsymbol{m}^{\mathrm{B}} + \tau \boldsymbol{m}^{\mathrm{T}}|} \right), \quad (11)$$

where $\tau \in [0, 1]$, while the denominators are never zeroing due to the last inequality in (10). As it follows from the above, the fundamental (the first) homotopy group of X is trivial:

$$\pi_1(X) \cong \pi_1(\mathbb{S}^2) = 0. \quad (12)$$

This implies that the model does not support topologically stable vortices, which entirely agrees with our observation in the numerical experiment.

B. Higher order homotopies

Assuming that the Heisenberg exchange represents, as usual for most of the ferromagnets, the leading energy term, one should expect near-continuous variations of spins from site to site almost everywhere, except for point defects. Accordingly, the classifying map is

$$f:\ \mathbb{S}^2 \to \mathbb{S}^2. \quad (13)$$

The preimage of the map f in (13) represents a closed surface containing a point defect and, in accordance with the geometry of the lattice, allowing the shape of a prism [Fig. 6]. If we denote by $\hat{\mathbf{n}}$ the outer normal for any face of the prism, then the corresponding topological charge of a point defect can be determined by Kronecker integral:

$$Q_{\mathrm{D}} = \frac{1}{4\pi} \oiint dS\ \mathbf{F} \cdot \hat{\mathbf{n}}, \quad (14)$$

where

$$\mathbf{F} = \begin{pmatrix} \mathbf{m} \cdot [\partial_y \mathbf{m} \times \partial_z \mathbf{m}] \\ \mathbf{m} \cdot [\partial_z \mathbf{m} \times \partial_x \mathbf{m}] \\ \mathbf{m} \cdot [\partial_x \mathbf{m} \times \partial_y \mathbf{m}] \end{pmatrix} \quad (15)$$

is the vector of curvature[10,39] and x, y, z are local right-handed Cartesian coordinates, defined in each face of the prism such that $\hat{\mathbf{r}}_3 \cdot \hat{\mathbf{n}} = 1$. Equivalently, Q_{D} can be calculated by the Berg and Lüscher method[40] on the triangulated prism surface.

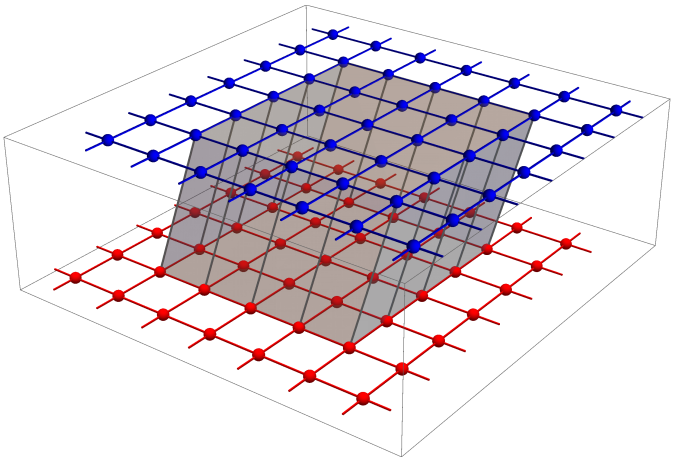

FIG. 6. Sketch of a prism-shaped surface that encloses a point defect.

The topological invariant (14) is similar to that of a Bloch point[31], a magnetic point defect in the bulk systems. The key difference is that in bulk, the convex surface S, over which the integration is performed, can formally be extended to a sphere with the diameter tending to infinity, while, in our bilayer system, S is always confined by two layers.

Remarkably, the topological index of such a point defect, besides Eq. (14), can also be expressed in terms of skyrmion topological charges of the top layer, Q^{T}, and the bottom layer, Q^{B} given by

$$Q_{\mathrm{T,B}} = \frac{1}{4\pi} \int dx\ dy\ \mathbf{m}^{\mathrm{T,B}} \cdot [\partial_x \mathbf{m}^{\mathrm{T,B}} \times \partial_y \mathbf{m}^{\mathrm{T,B}}], \quad (16)$$

The skyrmion classifying map corresponds to the second homotopy group of the sphere:

$$g:\ I^2/\partial I^2 \to \mathbb{S}^2, \quad (17)$$

where I^2 is a rectangle in one of the layer and ∂I^2 – its perimeter. Note that the domain can be chosen in any other way while remaining homeomorphic to a rectangle. The one-point compactification of the rectangle is possible due to the fixed magnetization value along its perimeter, $g(\partial I^2) = \mathbf{m}_0$. The preimage of the map g is homeomorphic to the two-sphere, $I^2/\partial I^2 \cong \mathbb{S}^2$, so the Eq. (17) is effectively a map from one two-sphere to another as in (13). The corresponding topological charges

of skyrmions can be found again using the Kronecker integral (or Berg and Lüscher method) but on a flat domain:

$$Q_L = \frac{1}{4\pi}\int dS\ \mathbf{F}\cdot\hat{\mathrm{e}}_z, \tag{18}$$

where L defines the top or bottom layer (T or B). Note that formulas (18) and (16) are equivalent.

From (14) and (18) follows the connection between the topological charge of the point defect and skyrmion charges in the top and bottom layers:

$$Q_{\mathrm{D}} = Q_{\mathrm{T}} - Q_{\mathrm{B}}. \tag{19}$$

The contribution from the side facets of a prism vanishes in Eq. (19) because of fixed magnetization, $\mathbf{m}_0$, at the periphery. In other words, the magnetization at the side facets of a prism represents a collinear state with $\mathbf{F} = 0$.

S2. FIRST-PRINCIPLES STUDY

Here we consider the interface between a layered structure of fcc InAs as the source of SOC and a Ni (Fig. 7). For simplicity, we consider three layers of In and single layers of Ni. We add an additional layer of Ni (Blue sphere in Fig.7) in the bottom to symmetrise the structure. The relaxed structure possesses an in-plane lattice vector 4.268Å.

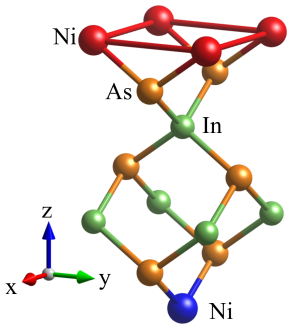

FIG. 7. Lattice structure of symmetrised NiInAs thin film.

The effective magnitudes of exchange (J) and DMI (D) are calculated from the dispersion of the spin spiral for Ni on the top surface. The total energy of the spin spiral for different q vectors are calculated with generalised Bloch theorem with $48\times48\times1$ k-points. For $\boldsymbol{q} = (0,0,0)$, the magnetic moment of Ni on the top surface is oriented in the x direction in the plane, while the magnetic moment of Ni on the bottom surface is oriented in the y direction. Thus, only the q-dependence of the magnetic moment of Ni on the top surface can be considered since the magnetic moments of upper and lower Ni are perpendicular to each other. To obtain the exchange parameter (J) we calculate the dispersion for spin spiral without SOC which results in a symmetric dispersion ($E(q)$=$E(-q)$). The exchange coupling can be obtained by exploiting the relation $E(q) = -\sum_n J_n \cos(2\pi nq) + E_0$, where the suffix n corresponds the coupling between n^{th} nearest neighbour. To obtain the DMI, we introduce SOC and calculate the energy due to SOC. This contribution is odd in q ($E(q)$=-$E(-q)$) and different orders of DMI can be obtained by fitting it with $E(q) = -\sum_n D_n \sin(2\pi nq)$. The values obtained for J and D along x and y direction considering upto 8 nearest neighbours are shown in Table I.

	1	2	3	4	5	6	7	8
J_x	1.41	0.38	0.17	0.04	-0.08	-0.06	0.08	-0.10
J_y	1.61	0.37	0.09	-0.12	-0.23	0.03	0.36	-0.35
D_x	0.01	0.01	0.01	0.00	0.00	0.00	0.00	0.00
D_y	0.09	0.06	0.05	0.00	-0.01	-0.00	0.01	-0.00

TABLE I. J and D parameter (in meV) along x and y direction.